EFFICIENT AEROELASTIC ANALYSIS OF INFLATABLE STRUCTURES USING ENHANCED POTENTIAL FLOW AERODYNAMICS

Enrique Ortega[1], Roberto Flores[2,3], Eric Cuartero[4] and Eugenio Oñate[3]

[1]Serra Hunter professor at Escola Superior d'Enginyeries Industrial, Aeroespacial y Audiovisual de Terrassa, Universitat Politècnica de Catalunya. Colom 1-11, 08222 Terrassa, Spain.

[2]Escola Superior d'Enginyeries Industrial, Aeroespacial y Audiovisual de Terrassa, Universitat Politècnica de Catalunya. Colom 1-11, 08222 Terrassa, Spain.

[3]Centre Internacional de Mètodes Numèrics en Enginyeria (CIMNE). Gran Capità s/n, 08034 Barcelona, Spain.

[4]BuildAir Inflatable Structural Solutions. Av de Barcelona 40, 08970 Sant Joan Despí, Barcelona, Spain.

Abstract. An efficient method for the aeroelastic analysis of wind effects on inflatable structures is presented. The solution scheme is staggered and uses an explicit finite-element structural solver and potential flow aerodynamics. In order to take into account the essential features of the flow around blunt-shaped structures, a physics-based correction of the inviscid solution is proposed. The procedure involves automatic prediction of the detached flow areas (using Stratford's criterion) and an empirical modification of the calculated pressure field intended to match the real viscous behavior. Several validation benchmarks and a realistic application example are presented. The results show the capability of the model to predict the wind loads on the structure with sufficient accuracy and low computational cost, making it possible to use aeroelastic analysis for routine calculation of inflatable structures.

Keywords. Inflatable structures, wind loads, potential flow, viscous corrections.

1 INTRODUCTION

The discovery of new polymeric materials in the sixties triggered a rapid development of inflatable structures. The new materials enabled application of these structures to new and diverse fields. The success of inflatable structures stems mainly from the reduced amount of material needed to contain a given working volume. This results in low weight, efficient packaging and high portability. Furthermore, inflatable structures allow lower fabrication and maintenance costs with respect to conventional construction, while retaining reasonable service life and resistance to harsh environments. These characteristics have boosted the popularity of inflatables, which today have a wide range of applications in several fields, such as civil, naval and aerospace engineering, architecture, arts, entertainment and advertising, see for instance [1-6].

From the point of view of the analysis and design, inflatables present several specific challenges, such as the characterization of the materials and structural response (which are highly nonlinear), airtightness and shape stability in complex structures. In addition, multiple safety issues (e.g. fire, snow and wind) must be considered, often with a level of complexity exceeding the scope of standard analysis techniques developed for conventional structures. A typical case is the study of wind-induced phenomena. Since inflatables allow larger deformations and have a low inertial mass, the interaction between the structural deformations and the aerodynamic loads is potentially much more important than in stiffer structures. Traditionally, these effects have been studied experimentally (from simple in-situ measurements to costlier wind tunnel tests), but in the last decades numerical simulation is playing an increasingly important role [7].

The first numerical tools for fluid-structure interaction (FSI) analysis of inflatables date back to the early nineties, and were mainly intended for the simulation of parachutes. In these works, the air is modeled with potential flow and panel methods while finite element (FE) techniques are used for the structure. Since discretization of the surrounding fluid is not required in panel methods, the solution procedure is drastically simplified. This methodology has proven very effective for parachute analysis, particularly when applied to streamlined shapes where the flow is mostly attached [8-11]. More recently, panel methods have been also used for solving inflatable devices like airbags [12-14], but the application to external aerodynamics problems is quite limited due to flow detachment. Nonetheless, this issue can be still solved in the context of inviscid aerodynamics with the help of vortex methods [15-17]. These use free particles to model the vorticity in the boundary layers and wakes, without resorting to body-fitted grids for the entire fluid domain. This local meshless approach treats viscous effects and flow separation effectively. Although vortex methods have been applied mainly for parachute simulation [18], the increasing complexity of current numerical problems have turned this approach also attractive in other fields of science and engineering [17, 19, 20].

Higher-fidelity FSI methods with full volume discretization allow for a more detailed modeling, but at the expense of a much higher computational cost. Typical approaches use interface-tracking and interface-capturing techniques; as well as embedded grids [21-23]. Among them, a remarkable family of methods emerged in the context of the deforming-spatial-domain/stabilized space-time (DSD/SST) technique [24, 25]. There are also different partitioned approaches that have been developed for inflatable membrane structures [26, 27],

meshless techniques [28, 29] and numerous successful applications of commercial software such as LS-DYNA® [30], Ansys® CFX [31], Fluent [32], Tdyn [3] and Abaqus [6].

In the context of practical design, time and computer resources are limited and multiple studies are often required to assess sensitivities. Hence, methods that yield acceptable accuracy while minimizing the solution cost are necessary. This is especially important, because many of the companies manufacturing inflatable structures are work with tight budgets. Furthermore, the potential users of the analysis software usually have little training in continuum mechanics and numerical analysis, and this necessitates simple modeling approaches with minimal user intervention. To reach this balance, the International Center for Numerical Methods in Engineering (CIMNE) and the Escola Superior d'Enginyeries Industrial, Aeroespacial i Audiovisual de Terrassa (ESEIAAT) have been developing efficient design tools, mainly intended for ram-air parachutes. The solution approach is based on potential flow aerodynamics (a low-order panel method), explicit FE structural dynamics and staggered FSI coupling; see [33] and recent validation results in [34]. In the present work, this methodology is extended for the simulation of wind effects on inflatable structures. To this end, the special features of the flow around blunt body shapes are taken into account by applying semi-empirical corrections to the inviscid flow field. The goal is to simulate the main features of the real flow while keeping the efficiency of the underlying inviscid solver. The proposed methodology is described in Sections 2 and 3, and several numerical examples are presented in Section 4 to illustrate the performance achieved. The most relevant conclusions are outlined in Section 5.

2 OVERVIEW OF THE SIMULATION APPROACH

The solution methodology was described in [33] and the especial features implemented to address practical requirements in the simulation of inflatable structures are summarized below.

2.1 Structural modeling

The structural solver is based on a large-displacement dynamic FE formulation. Since cables and membranes lack bending stiffness and buckle under compressive loads, a wrinkling model is used to correct the elemental stresses. When computing stresses small tensile strains are assumed, but arbitrarily large compressive strains are allowed to account for wrinkling. The equations are advanced in time with an explicit second-order scheme. While this integrator is only conditionally stable (thus limiting the time increment) it is robust and efficient when applied to highly nonlinear problems. A numerical dissipation model with Rayleigh damping and bulk viscosity is used to control local high-frequency modes that are not well resolved by

the staggered coupling adopted. While simple and inexpensive, this approach requires attention while setting the damping parameters to prevent spurious effects on the results. More specifically, the mass-proportional damping term has, by far, the greatest potential for contaminating the solution. Some guidelines for tuning these parameters are given in [33, 35].

The solver models cables, membranes and 3D solids using 2-node linear, 3-node triangular and 4-node tetrahedral elements, respectively. When applied to inflatable structures, line elements are used for simulating the structure anchoring and stabilization cables, also the fabric seams and reinforcement tapes. The fabric is modeled with triangle elements; if the mesh contains quadrilaterals (this choice is often preferred for aerodynamic purposes) these are automatically split into triangles for analysis. The solid tetrahedral elements model ballasts and any other suitable components. If the deformations of the parts discretized with volume elements are small in comparison with the rest of the structure, groups of solid elements can be lumped into rigid bodies to reduce the number of degrees of freedom.

Different types of kinematic constraints and analytical contact with pre-defined surfaces are available to accommodate the different support conditions found in real life. In addition, it is possible to prescribe time-varying tube pressurization (for inflation and deflation analyses) and several types of distributed loads (e.g. fixed-direction and follower) to simulate wind and snow actions.

2.2 Aerodynamic modeling

The flow solver is a low-order unsteady panel method with doublets and sources. The constant strength panels lower the complexity and computational cost. In addition, the discretization is simpler because exact matching between panels is not required. In order to model the wake, a time-steeping technique is used to account for rollup. Unsteady added mass effects are also simulated; and drag forces on cables and simple bodies can be accounted for by means of experimental coefficients and functions easily obtained from the literature. For the present work, the unsteady capabilities of the solver have not been used. All the results presented come from steady-state computations.

In order to model the effects of atmospheric boundary layers, an exponential wind profile has been implemented according to the Eurocode 1 standards (EN 1991-1-4: wind actions, see [36]). Notice that, in the context of potential flow, atmospheric boundary layers can be approximated as a constant far-field inflow velocity plus a local velocity correction at the

surface of the structure that depends on the distance to the ground. Hence, the far-field irrotational flow is preserved.

Although simple and effective, the inviscid solution approach described is only suitable for solving smooth flows (i.e., over streamlined bodies). Since viscous detachment cannot be neglected in blunt inflatable structures, a methodology to include this effect on the computed loads is presented below.

3 FLOW DETACHMENT CORRECTION

High-Reynolds flows around blunt bodies are characterized by extensive and well-defined areas of detached flow. In these problems, experiments show that the velocity and pressure fields on areas where the boundary layer remains attached do not differ much from an inviscid solution. The differences arise when the flow separates. Then, the pressure recovery downstream of the separation point stops and the time-average pressure in the near-wake becomes almost constant. Since in blunt body problems pressure is the main contribution to the aerodynamic forces, these experimental observations suggests a simple correction of the inviscid solution. First, at the beginning of each time step, the inviscid solution is used to predict the flow separation points. Next, the inviscid pressures downstream of the detachment area are corrected by keeping their value constant. Finally, the corrected pressure field is smoothed and transferred to the FE solver to calculate the structural response. It should be noted that smoothing is not strictly necessary, as it has little effect on the overall loads used for sizing. However, 2-3 passes are convenient to ensure a smooth pressure field in the detached area, especially when coarse grids are employed. The smoothing procedure uses nodal pressure averaging with element area weighting.

In order to determine where the flow around a body is likely to detach, there are numerous methods in the literature that combine approximate boundary layer solutions and empirical data to derive practical separation criteria [37, 38] . In this work, Stratford's method [39] is used. It is fast to compute and reasonably accurate. Furthermore, it only requires the inviscid pressure distribution on the body. Since Stratford's separation criterion was developed for two-dimensional and axisymmetric problems [40], it is applied along the flow streamlines. The procedure presented accounts for fully turbulent and laminar-turbulent flows (using Michel's transition method [41]) and yields an averaged (quasi-steady) pressure field accounting for flow separation effects. The main implementation details of the method are described next.

3.1 Streamline calculation

The first step for the correction of the inviscid solution is to recover the flow streamlines. To this end, the inviscid solver provides the instantaneous velocity and pressure at the center of each panel in the body surface (triangles or quadrilaterals). The velocity field is normalized and a linked-list is constructed to identify, for each surface panel *i*, its corresponding downstream panel *i+1*. The latter is the neighboring panel *j* that maximizes $\left(\Delta_{ij} \cdot \widehat{\boldsymbol{U}}_i\right)$, where $\Delta_{ij} = \left(\boldsymbol{x}_j - \boldsymbol{x}_i\right)/\left|\left(\boldsymbol{x}_j - \boldsymbol{x}_i\right)\right|$ is the unit vector linking the panels' centers and $\widehat{\boldsymbol{U}}_i$ denotes the normalized velocity vector at *i*. The search is performed over the nearest panels, skipping those already tagged. Panels where flow reversal takes place are also marked at this stage.

Using the linked-list above, the streamlines are constructed starting from the forward stagnation areas until there are no remaining downstream panels or flow reversal occurs (which indicates the rear stagnation area has been reached). In this way, the panel entries along each streamline are ordered in the flow direction and ready for application of Stratford's criterion. The additional information needed for finding the separation points is the location of the panels' centers $\boldsymbol{x}_i$, their velocity modulus U_i (which corresponds to the velocity at the outer edge of the boundary layer) and pressure coefficients Cp_i.

3.2 Prediction of separation points

Stratford's model predicts the detachment of incompressible high-Reynolds flows using a two-layer approach. Closer to the surface, in the inner part of the boundary layer, the pressure forces are balanced with the gradient of the viscous shear-stress (inertial forces are negligible). In the outer layer, on the other hand, the flow is assumed nearly inviscid, and the pressure forces are balanced against inertial forces by variation of the dynamic pressure. The model formulation and several validation examples are given in [39]. Extensions to account for compressibility effects can be also found in [38]. In the present work, the guidelines given in [37, 42] are followed with the objective to emphasizing the implementation aspects.

Following with the data described in the previous section, it is assumed that the points $\boldsymbol{x}_i$ along each streamline can be connected by straight lines, so that the distance between them is approximately the Euclidean distance between the panels' centers $\boldsymbol{x}$ (the surface discretization is considered smooth). Hence, in coordinates along the streamline, the first point (stagnation point) is located at its origin, i.e. $x_0 = 0$, and the position of the downstream points *i = 1,2,…n* is calculated as $x_i = x_{i-1} + |(\boldsymbol{x}_i - \boldsymbol{x}_{i-1})|$. Using these coordinates, the position of the point of maximum velocity x_m can be also determined. In addition, since the boundary layer can start

laminar and then become turbulent, a transition location $x_t < x_m$ at which the flow suddenly switches to fully turbulent is introduced in the analysis. This can be prescribed (user-input) or calculated with a suitable transition criterion. The downstream position of the separation point x_s is the problem solution. All these points characterizing the actual boundary layer under analysis are plotted in Figure 1 against $(1 - \bar{C}p_i)$. Here, $\bar{C}p_i$ is the pressure coefficient at a point x_i, referred to the conditions at the point of maximum velocity x_m. It is calculated as $\bar{C}p_i = (p_i - p_m)/q_m = 1 - q_i/q_m$, where p_i and q_i are the static and dynamic pressures at x_i and p_m and q_m are the same variables measured at point x_m. The function $(1 - \bar{C}p_i)$ is zero at the forward stagnation point, one at the point of maximum velocity and go back to zero at the rear stagnation point in an ideal case with complete pressure recovery.

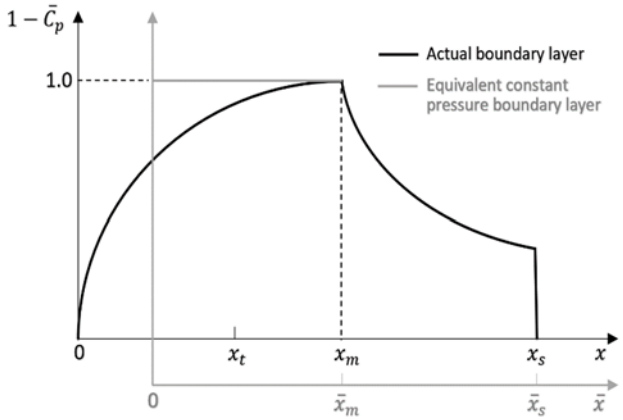

Figure 1. Actual and equivalent pressure distributions along a streamline and characteristics points [42].

An additional coordinate system $\bar{x}$ is depicted in Figure 1. It is intended for more general analyses accounting for boundary layer transition and favorable pressure gradients in the turbulent region (the original criterion only applies to fully turbulent boundary layers with adverse pressure gradients). To this end, Stratford made the assumption that at $x = x_m$ the actual velocity profile can be assimilated to that of a flat-plate turbulent boundary layer whose leading edge is located at a downstream position $\bar{x}_0 = x_m - \bar{x}_m$. Hence, $\bar{x}_m$ is the length of an equivalent constant pressure region over which a turbulent boundary layer would develop the same momentum thickness θ as the actual laminar-turbulent boundary layer over the distance x_m. The velocity profile at this point is approximated by a power-law $u/U_m = (y/\delta)^{1/n}$. With these considerations, the Stratford's criterion for obtaining the location of the separation point can be expressed as [42]

$$\left(2\bar{C}_p\right)_s^{(n-2)/4}\left(\bar{x}\frac{d\bar{C}_p}{dx}\right)_s^{1/2} = N\beta\left(10^{-6}\overline{\mathrm{Re}}\right)^{1/10}, \qquad (1)$$

where subscript s indicates values measured at the separation point. $\overline{Re} = (U_m \bar{x}_m)/\upsilon$, with υ denoting the fluid kinematic viscosity, and

$$N = 11.36 \frac{(n-2)^{(n-2)/4}}{(n+1)^{(n+1)/4}(n+2)^{1/2}} \ . \tag{2}$$

In Eq. (1), the experimental parameter β depends on the shape of the boundary layer near separation. Values of $\beta = 0.66$ and 0.73 are suggested in [39] for cases where $d^2\bar{C}p/dx^2 < 0$ and $d^2\bar{C}p/dx^2 \geq 0$, respectively. The parameter n determines the shape of the equivalent boundary layer at $\bar{x}_m$, but it has not a marked effect for typical applications where $6 \leq n \leq 8$. Following [42], a value $n = 6$ is adopted here. It should be noted that other values of n may affect to some extent the validity of the separation criterion because of the formal restriction $\bar{C}p \leq (n-2)/(n+1)$ imposed in the model to join the inner and outer layers. Using the parameters described, Eq. (1) becomes [42]

$$\frac{\left(2\bar{C}_p\right)_s \left(\bar{x}\frac{d\bar{C}_p}{dx}\right)_s^{1/2}}{\left(10^{-6}\overline{\mathrm{Re}}\right)^{1/10}} = S(x) = \begin{cases} 0.35 & \text{for} \quad d^2\bar{C}_p/dx^2 < 0 \\ 0.39 & \text{for} \quad d^2\bar{C}_p/dx^2 \geq 0 \end{cases} \tag{3}$$

Experimental observations show that *S(x)* increases as detachment is approached and decreases after separation. Therefore, Eq. (3) is evaluated at each point x_i along the streamline starting from x_0, and separation is predicted where *S(x)* reaches the indicated values. Some authors proposed to increase slightly *S(x)* to counteract the tendency of Stratford's method to predict early separation. A value about *S(x)*≈0.5 is suggested in [40, 43] to improve the agreement with experiments. The effects of this change are explored in Section 4.

The first and second derivatives of $\bar{C}p$ in Eq. (3) are calculated using second-order forward, central and backward differences. To this end, since the points x_i are not equally spaced along the streamline, a second-order polynomial is fitted around the point of interest and the derivatives are then computed from the latter (finite differences by polynomials [44]). Higher-order approximations were also tested, but they had a very limited impact on the results.

Regarding the length of the equivalent boundary layer $\bar{x}_m$ needed to calculate $\overline{Re}$ in Eq. (3), [42, 43] suggest the following approximation for laminar-turbulent boundary layers

$$\bar{x}_m = 38.2\left(\frac{\upsilon}{U_t x_t}\right)^{3/8}\left[\int_0^{x_t}\left(\frac{U}{U_t}\right)^5 dx\right]^{5/8} + \int_{x_t}^{x_m}\left(\frac{U}{U_m}\right)^3 dx \ , \tag{4}$$

where the transition location x_t can be defined by the user or determined from the actual flow conditions using a suitable transition criterion. Michel's method [41] is employed here. It is based on a correlation for the local momentum thickness given by

$$\mathrm{Re}_{\theta,\mathrm{t}} = \frac{U(x)\theta(x)}{\upsilon} \approx 2.9\,\mathrm{Re}_{x,t}^{0.4} \ , \tag{5}$$

where the subscript t denotes values measured at x_t and the momentum thickness at each station $\theta(x)$ can be calculated, for example, using Thwaite's method [42]

$$\theta(x) = \frac{0.45\upsilon}{U_m^6}\int_0^x U^5(x)dx \ . \tag{6}$$

A modified version of Eq. (5) is proposed in [45]. This correlation, valid for Reynolds number between 0.1 to 40 million, is given by

$$\mathrm{Re}_{\theta,\mathrm{t}} \approx 1.174\left[1+\frac{2.24\times10^4}{\mathrm{Re}_{x,t}}\right]\mathrm{Re}_{x,t}^{0.46} \ . \tag{7}$$

Although a more extensive analysis would be necessary, initial tests using Eqs. (5) and (7) in cases of smooth flows have led to similar results. The integrals in Eqs. (4) and (6) are calculated along the streamline using the trapezoidal rule.

Finally, it is important to note that the separation distance $\bar{x}_s$ predicted by Eq. (3) must be corrected to take into account the actual boundary layer length. Since $\bar{x}_s - \bar{x}_m = x_s - x_m$ (see Figure 1), the real separation distance is $x_s = x_m + (\bar{x}_s - \bar{x}_m)$.

4 NUMERICAL RESULTS

Several application examples are presented in this section. First, four validation benchmarks are intended to assess the flow correction and discuss the relevant parameters. The models employed are rigid and range from simple bodies to a more representative open shelter structure. The final example is a realistic test where the methodology is applied to the coupled aeroelastic solution of an inflatable hangar subject to steady lateral wind.

4.1 Validation examples I: basic flows

The first test case is a circular cylinder in crossflow. The model has diameter $D = 1$ m, span $b = 5$ m and endplates are used to make the flow two-dimensional. The discretization consists of 1553 quadrilateral panels and the simulations involve supercritical flows with Reynolds numbers $Re_D = 0.73$, 3.49 and 8.27 million. Laminar-turbulent and fully-turbulent flows are considered. The results are compared with experimental data given in [46] for a Mach number

$M = 0.177$. Figure 2 shows the tests model with the calculated detached flow area (colored in red) and the resulting Cp distribution (i.e. after detachment correction). The wind flows in the positive x-direction.

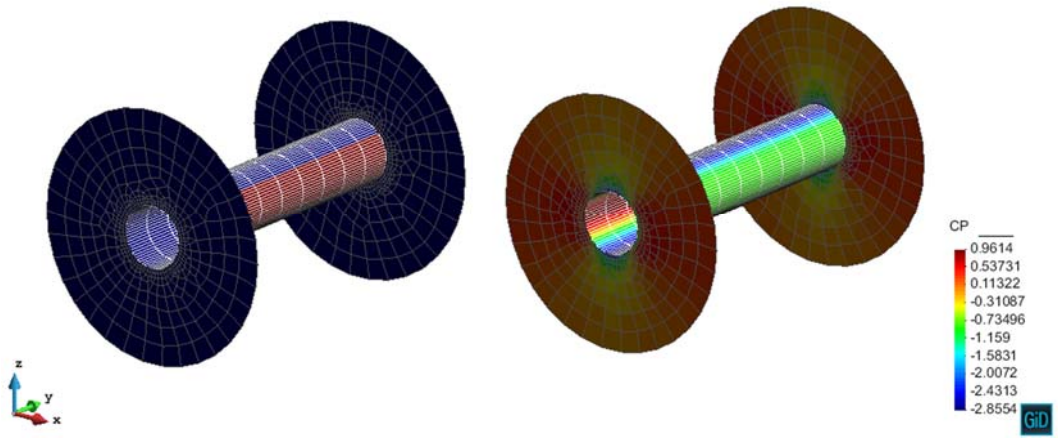

Figure 2. Circular cylinder at Re=3.49M. Detached flow area (colored in red, left) and corrected Cp distribution (right).

The pressure distribution on a cylinder cross-section is compared with experimental data in Figure 3 (θ is measured clockwise from the leading edge). The assumption of an initially laminar boundary layer that transitions to turbulent further downstream is satisfactory for $Re_D = 0.73 \cdot 10^6$, but fully-turbulent flow yields better results for higher values of Re_D. The figure demonstrates improved agreement with experimental results using the separation criterion $S(x) \geq 0.5$ [39, 43]. In such case, differences between the calculated and experimental pressure distributions are below 10%.

Figure 4 illustrates the evolution of the separation point and the pressure drag of the cylinder (the experimental C_D values correspond to those obtained from integration of static pressures in [46]). For the cases studied, a laminar-turbulent boundary layer with transition at the suction peak is considered (tests with other transition criteria showed no appreciable differences on the results). The calculated separation point reasonably matches the experimental trend for $Re_D =$ 0.73 and 3.49M, and the maximum difference in C_D is about 10% for the results obtained with $S(x) = 0.5$. However, a low sensitivity of the predicted separation point to changes in Re increases the differences for $Re_D = 8.27$M. This may be caused by the transition criterion adopted, but also because Stratford's variable $S(x)$ in Eq. (3) is more sensitive to the shape of the pressure distribution (which is the same for all the cases studied) than the Re number. If the inviscid pressure distribution fails to model the actual flow features outside the boundary layer

(mainly magnitude and position of the suction peak), an important part of the Re effects could be lost, causing the accuracy of the prediction method to degrade.

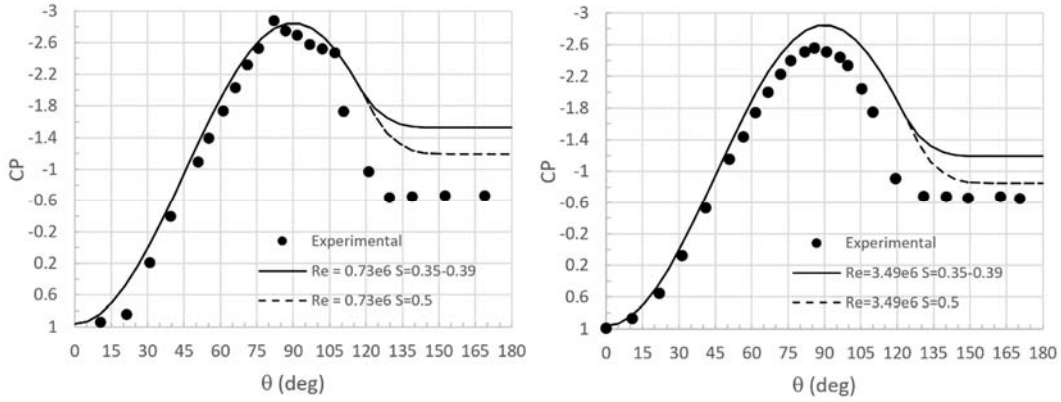

Figure 3: Experimental and calculated Cp distributions for a circular cylinder in crossflow using different limits for the Stratford's variable (0.35-0.39 and 0.5). Re = $0.73 \cdot 10^6$ (left) and Re $3.49 \cdot 10^6$ (right).

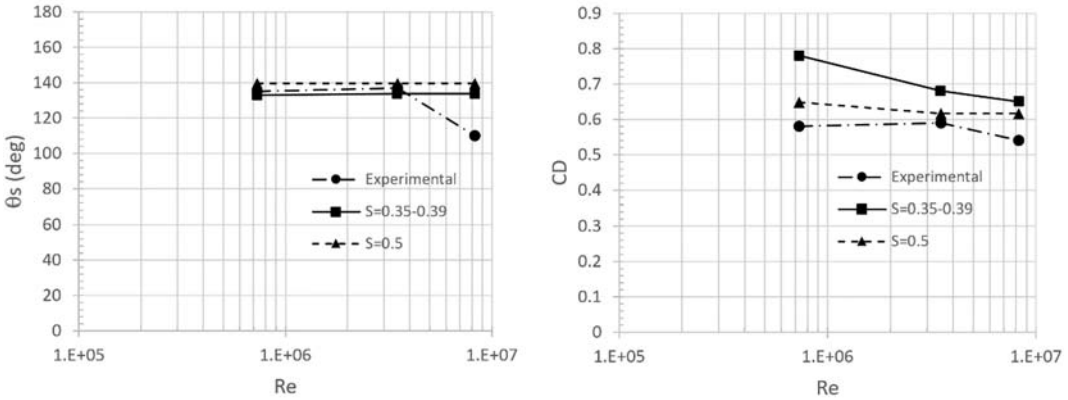

Figure 4. Evolution of the cylinder separation point (left) and drag coefficient (right) with Re number. In the solutions calculated for the different values of the Stratford's variable, the transition point is fixed at the suction peak and the calculated C_D only takes into account the pressure force contribution.

In this regard, lower accuracy can be expected in subcritical flows ($Re_D < 160 \cdot 10^3$), but errors in the inviscid Cp distribution can also affect high-Re flows, as shown in Figure 4. There, a transition closer to the stagnation point increases considerably the length and thickness of the turbulent boundary layer. This modifies the external flow field (far from the surface of the solid) causing differences with the potential solution, which does account for boundary layer thickness. Figure 5 illustrates this effect, showing the change in the experimental pressure distribution that occurs when Re increases from 3.49 to 8.27M. The suction peak reduces and there is early detachment, but the calculated solution cannot reproduce this trend (the maximum difference between calculated and experimental Cp increases up to approximately 30%). Although the separation point prediction can be improved by adjusting $S(x)$, the suction peak and the drag force would still be overestimated. As mentioned before, for the separation criterion to remain accurate the base Cp distribution (e.g., the inviscid solution in our case) must account for the relevant Re effects in the problem. In cases where the inviscid Cp deviates

considerably from the real pressure distribution, empirical pressure corrections based on the extent of the detached region could be applied upstream of the separation area to improve the accuracy.

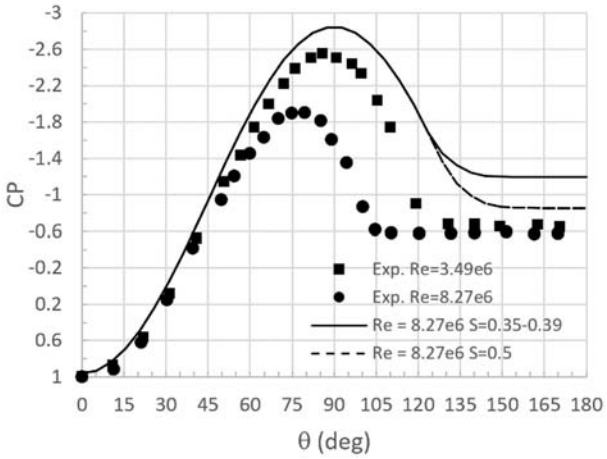

Figure 5. Effect of boundary layer thickening on the pressure distribution along a circular cylinder. Solid and dashed lines indicate numerical solutions calculated for different values of the Stratford's variable.

The next example involves an elliptical cylinder [47]. It has a minor-axis $D = 0.10$ m (3.98 in), major-axis $L = 0.30$ m (11.78 in) and span $b = 1.37$ m (4.5 ft). The flow disturbance caused by this body is smaller than in the previous example, and the boundary layer separates near the trailing edge. The discretization consists of 1362 quadrilaterals and the Reynolds number based on D is $139 \cdot 10^3$. A laminar-turbulent boundary layer is assumed, with transition at the suction peak (this is close to the value $x_t/D \approx 1.25$ found in the experiments). Figure 6 compares pressure distributions calculated for different values of $S(x)$. The agreement is satisfactory, and the criterion $S(x) \geq 0.5$ yields better results again. The maximum difference between the calculated and experimental Cp immediately after separation is about 12%, but then increases due to the appearance of flow reattachment in the experiment (not modeled by our method). The vertical dashed line in Figure 6 indicates the beginning of the experimental turbulent flow separation; the results in [47] show some scattering.

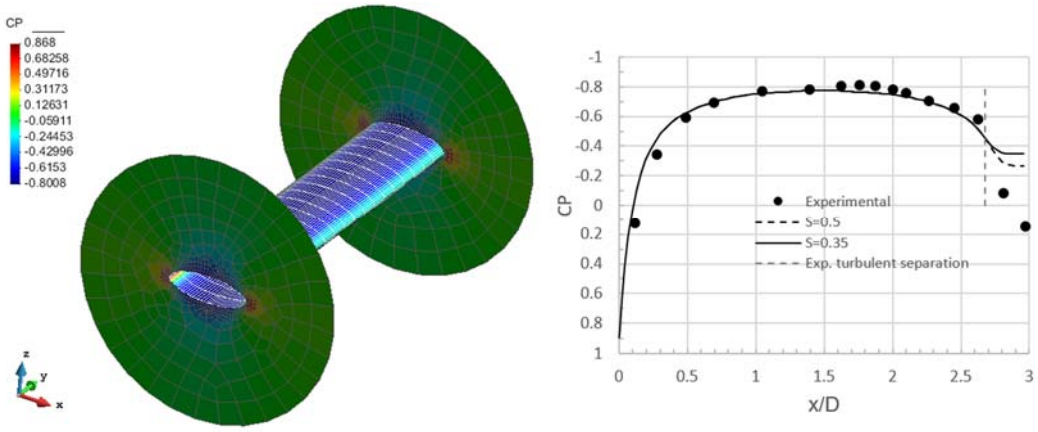

Figure 6. Elliptical cylinder in crossflow. Test model (left) and comparison of corrected Cp distributions with experimental results (right), Re_D=139K. Solid and dashed lines indicate the solutions obtained for different values of the Stratford's variable.

The third example involves the flow around a sphere. The model has 1297 quadrilaterals and the Reynolds number based on diameter is $420 \cdot 10^3$, near-critical and just after the drag crisis. The results are compared with experimental measurements from [48]. As shown in Figure 7, the computed pressure distribution has a small asymmetry (probably due to the unstructured grid used) and a slightly premature separation, as expected from Stratford's method. This increases the computed pressure drag, but its value is still within the range observed in the experiments. Based on the frontal area, the C_D calculated here is 0.22 (for $S(x) \geq 0.5$) and values between 0.12-0.25 are given in [48] for the total sphere drag (the contribution of viscous friction is small). Hence, taking into account the typical scattering found in drag measurements near critical Re, the results obtained are satisfactory.

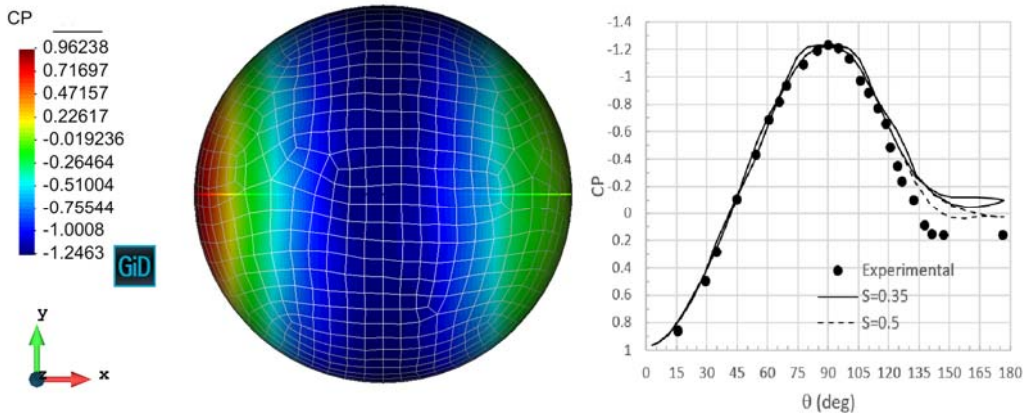

Figure 7: Flow around a sphere. Test model (left) and comparison of corrected Cp distributions (right) with experimental results, Re_D=420K. Solid and dashed lines indicate the solutions obtained for different values of Stratford's variable.

4.2 Validation example II: four-tube shelter model

The flow around a rigid shelter is solved here. The reference results are from wind tunnel tests conducted during the European research project uLites [49] at the Inter-University Research Centre on Building Aerodynamics and Wind Engineering (CRIACIV) [50]. The model has length $L = 0.225$ m, diameter $D = 0.450$ m and is made of four tubes 0.050 m in diameter each. The incident wind is a 5.5 m/s constant profile with different orientation angles. The resulting test Re based on the shelter diameter is $171 \cdot 10^3$. The discrete model has 14407 quadrilateral panels and a symmetry plane is used to simulate the ground surface (see Figure 8). The flow is considered fully turbulent and values $S(x) = 0.35 - 0.39$ are used in Stratford's method. This setting, which attempts to reproduce the effect of upstream atmospheric turbulence in the experiments, delivered better results near the critical value of Re_D.

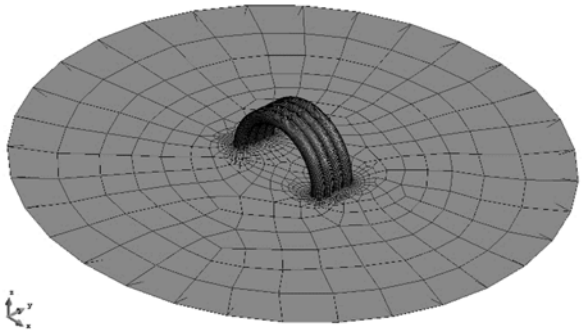

Figure 8. Four-tubes shelter discrete model and symmetry plane.

Lateral wind (β=90º) is considered first. Figure 9 shows the separated flow area and the corrected pressure distribution. The latter is checked against experimental results in Figure 10. The agreement along most of Tube 2 is quite satisfactory (suction zone and separation point), although the rear pressure recovery is overestimated (Figure 10, right). This might be due to discontinuities of the streamlines in the rear part of the tubes due to crossflow coming from the inner surface of the shelter, a zone that cannot be properly resolved with an inviscid model. However, note that the pressure differences apparent in Figure 10 (right) are not expected to have major impact on the overall loads, as they act over limited areas of the structure. More important is the effect of crossflow along Tube 1 (Figure 10, left). Although in the windward direction the flow detaches at about 120º, matching the experimental value, the numerical solution predicts a very low pressure area to the right of the separation point due to the high velocity of the air coming from the lower side as it flows around the tube. This causes an excessive pressure drop where the internal and externals flows intermix. Note that the flow pattern in the rear part of Tubes 1 and 2 is very complex because there is a combination of air

flowing from the lower side to the upper surface (circling around the edge of Tube 1) with impingement of the detached wake, which our model does not take into account.

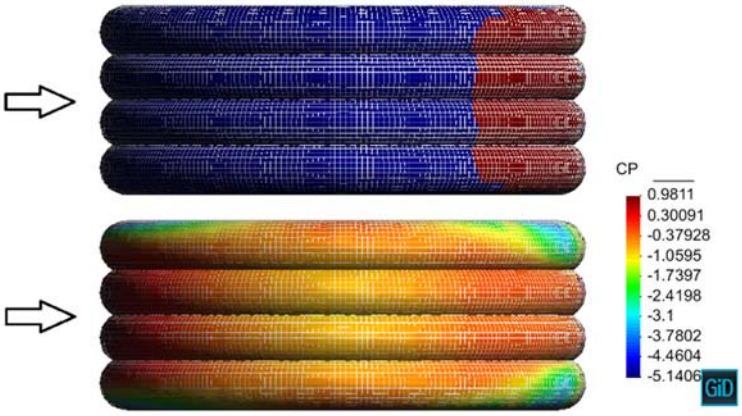

Figure 9: Detached flow zone (colored in red, top) and corrected Cp (bottom) calculated for β=90º.

In order to isolate the effects of the wind coming from the interior of the shelter (where the inviscid solution is not realistic), some tests have been performed using an enclosure. This consists of a couple of half-discs placed flush with the outer edges of Tubes 1 and 4, which resemble closely the effect of curtains acting as doors on a real hangar. The enclosure is intended to prevent the flow of air to pass from the lower side of the tubes (the interior of the hangar) to the upper surface, a phenomenon that in the open model creates an area of unrealistically high velocity on Tube 1. The results obtained show that using the enclosure the average magnitude of the Cp error on the separated region falls considerably, from 1.5 on the open model (Figure 10, left) to about 0.3 on the closed one (Figure 11). This seems a good modeling choice, yielding a reasonable approximation while remaining simple. It is important to stress that even higher-fidelity CFD methods struggle in this region, due to the unsteadiness of the flow field (see [50]).

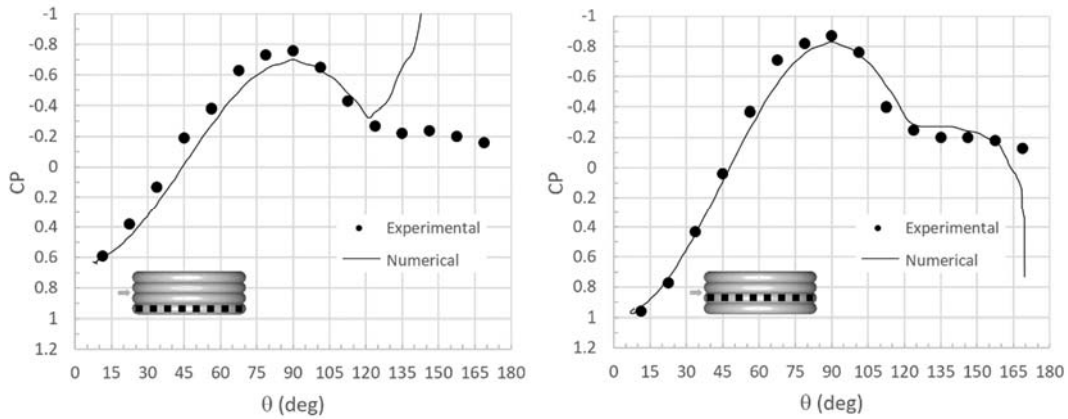

Figure 10. Experimental and calculated Cp distributions along Tube 1 (left) and Tube 2 (right), β=90º.

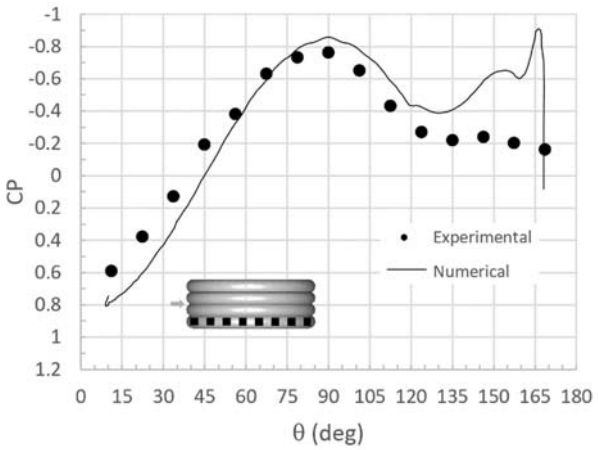

Figure 11. Cp distributions along Tube 1, β=90º (numerical results correspond to a closed model).

Oblique-wind (β=45º) effects are depicted in Figure 12 and Figure 13. The experimental data along Tube 4 (the windward cell) show early detachment (which could indicate near-critical flow) and a relatively low downstream pressure, probably caused by the air flowing longitudinally between the tubes (see Figure 13). The numerical solution shows a larger suction area with delayed detachment, and the downstream pressure is much lower due to high velocity air coming from the inner surface of the shelter (which is not well resolved by our method). The accordance along Tube 3 is better, although the rear pressure is somewhat reduced by the flow that detaches along the rear part of Tube 4. This effect also propagates, to a lesser extent, to Tubes 2 and 1. It should be noted that the experimental results in this example correspond to a relatively low Re number around the critical regime, where the accuracy of the separation criterion degrades. In addition, as explained above, the flow pattern in Tubes 1 and 2 is very complex due to the effect of the air flowing from the lower side of the hangar. There is also impingement of the detached wake from Tubes 3 and 4 and the effect of the ridges between tubes, which causes multiple instances of flow separation and reattachment (not taken into account by our model). However, it should be expected that a real hangar built with many more tubes (e.g. the H20 model of Section 4.3 has 11 tubes) will be much less sensitive to these inaccuracies, as they affect mostly the two tubes on the leeward side on the structure. In such cases, the relative size of the problematic area is smaller and the effect on the overall loads is limited.

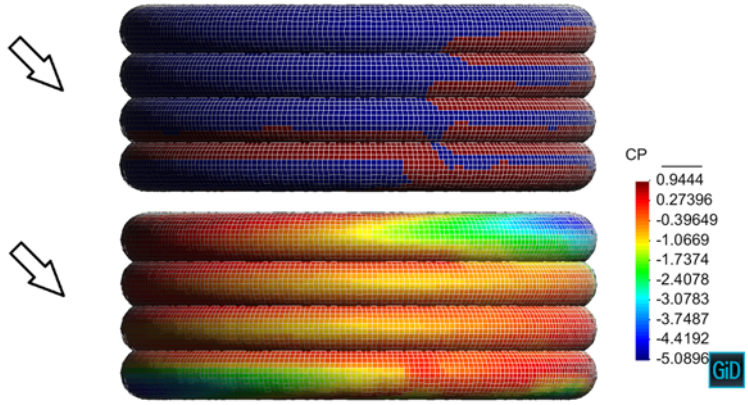

Figure 12. Detached flow zone (colored in red, top) and corrected Cp (bottom) calculated for β=45º.

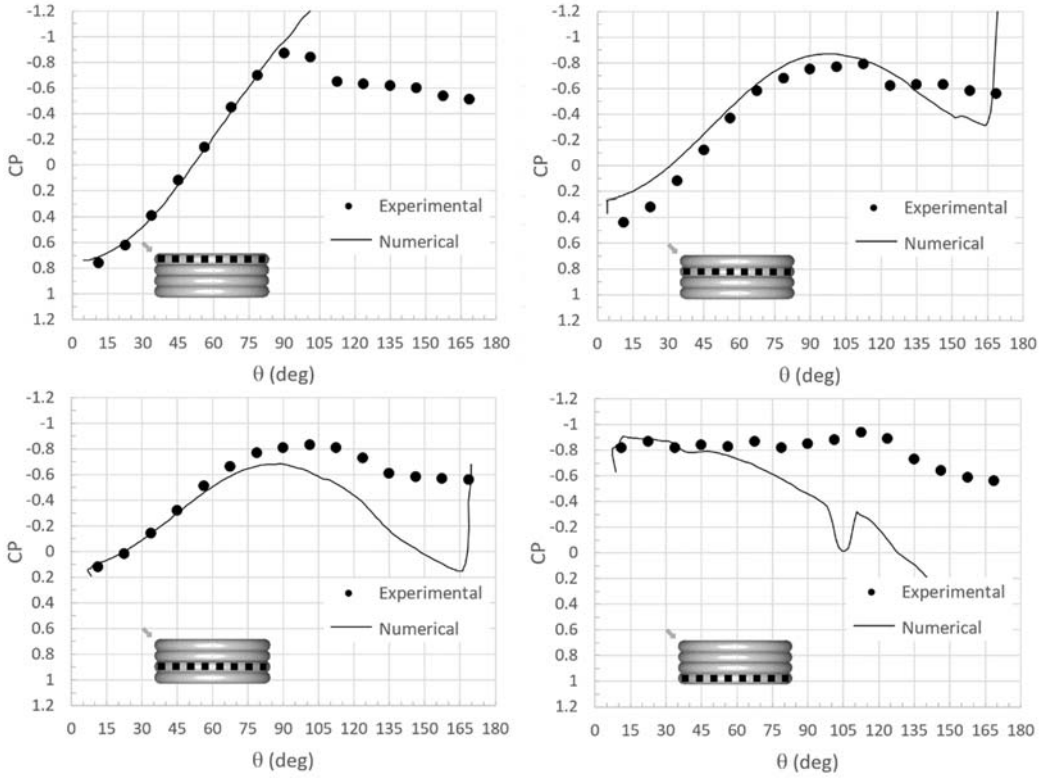

Figure 13. Experimental and calculated Cp distributions. From left to right: Tubes 4 and 3 (top) and Tubes 2 and 1 (bottom), β=45º.

Finally, longitudinal wind (β=0º) has been tested. In this case, the comparison appears severely affected by low-*Re* effects. Note that since the diameter of Tube 4 facing the wind is the length governing the flow separation process, the characteristic *Re* (about 19.10^3) is much lower than in the previous cases. The results are presented in Figure 13 and Figure 14. In the experiment, the flow around Tube 4 is clearly subcritical (θ_s < 80-90º [51]) and detaches prematurely. The pressure then remains almost constant downstream unless reattachment occurs (this is likely to happen to some degree downstream). As expected, the inviscid solution exhibits delayed separation, and this increases the suction along the shelter's outer surface (this is more evident

for the tubes closer to the separation point). The solution accuracy could be improved by adjusting the separation limits $S(x)$, or correcting the inviscid Cp distribution upstream the separation point. However, this particular problem is not expected for the larger Re values typical of full-scale structures.

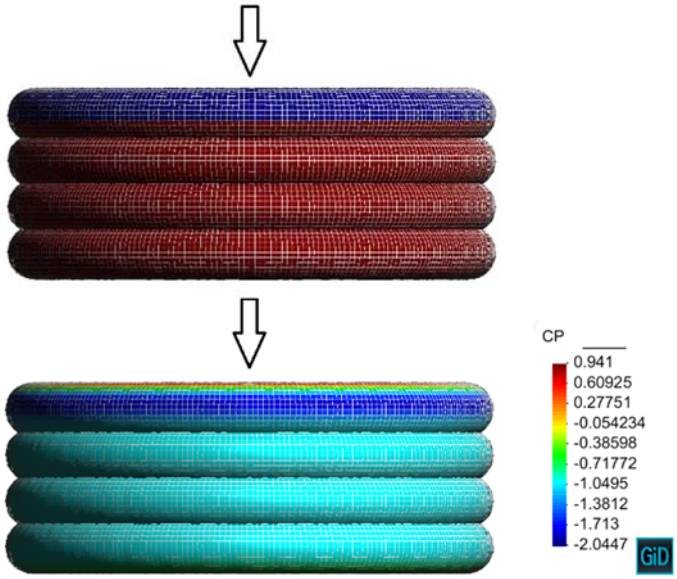

Figure 14: Detached flow zone (colored in red, top) and corrected Cp (bottom) calculated for β=0º.

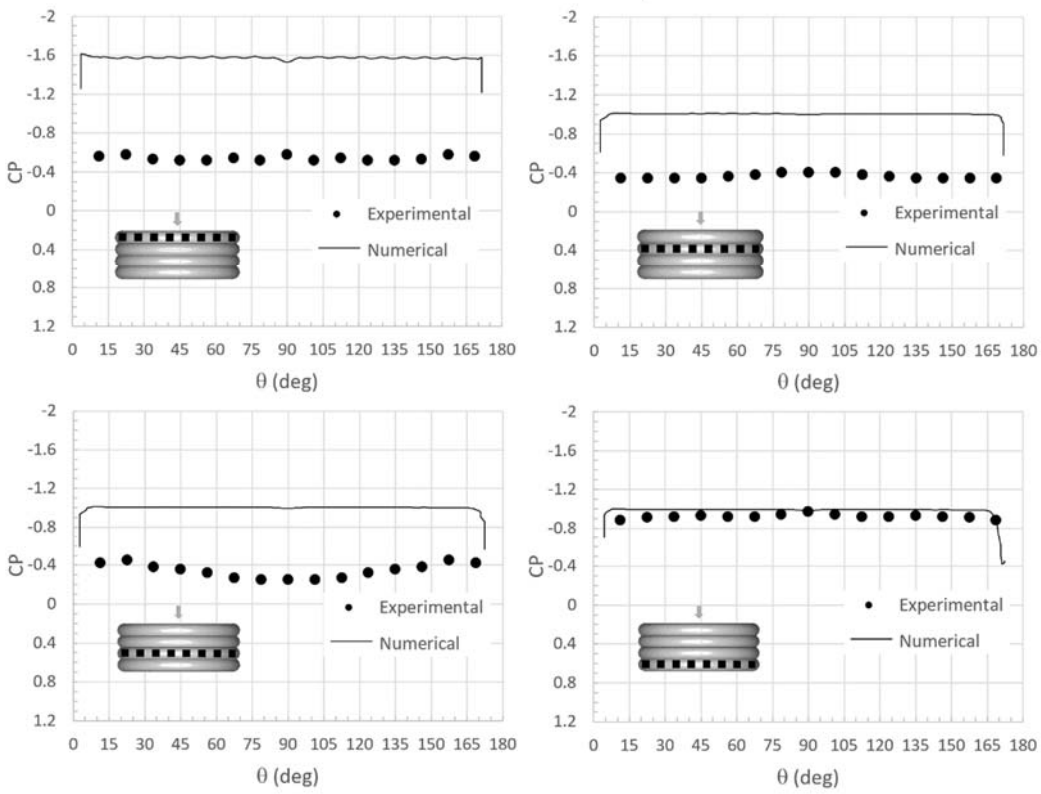

Figure 15: Experimental and calculated Cp distributions. From left to right: Tubes 4 and 3 (top) and Tubes 2 and 1 (bottom), β=0º.

4.3 Application example: two-way coupled solution of an inflatable hangar with wind loads

A Buildair's H20 inflatable hangar [52] subject to lateral wind (β=90º) is studied here. The hangar's internal width and height are 20.5 m and 10.25 m, respectively, and is made from 11 tubes (3.5 m in diameter each) that make up a total length of 31.2 m. In the discrete model, 21374 quadrilaterals are used for the fabric surfaces and 8014 line elements for the anchoring cables, fabric seams and reinforcements. A symmetry plane is included to model the ground surface. For the aerodynamic simulation, an atmospheric wind profile with basic velocity 90 km/h is prescribed according to the EN 1991-1-4 standards (the location of the hangar is supposed to be Barcelona, Spain). The Reynolds number based on the outer hangar's diameter is about $47 \cdot 10^6$. According to the previous results in high-*Re* flows, $S(x) = 0.5$ is used in Stratford's method and fully turbulent flow is assumed. The structure is attached to the ground at the corresponding anchoring points (treated as perfectly rigid) and a constant inflation pressure of 3000 Pa is applied to the tubes. The fabric is a pvc-coated polyester with a Young modulus of 0.38 GPa, 0.5 mm thickness and mass area density of 590 g/m^2. The reinforcements have a Young modulus of 2.5 GPa, 2mm thickness, 50 mm width and linear mass density 85 g/m; see [53] for further details. The model discretization is shown in Figure 16.

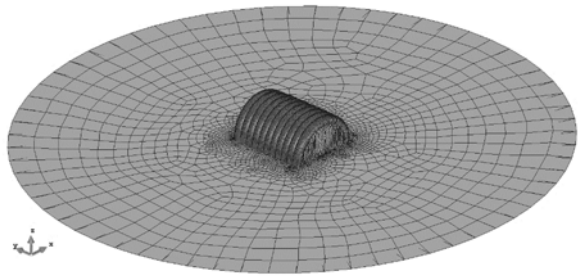

Figure 16. Buildair's H20 hangar discrete model and symmetry plane.

The goal of the analysis is to determine the steady-state deformations and stresses caused by the wind loads described above. The steady two-way coupled solution requires 26 s of physical simulation time. This takes about 1 hour CPU-time running in a desktop computer with Intel Core2 Quad Processor Q9550 @ 2.83 GHz (using 4 cores). The predicted flow separation area and the corrected pressure field are shown in Figure 17. The solution captures the main features of the flow around the hangar satisfactorily. Small higher-pressure areas can be also observed in the rear of the hangar. These are not totally removed by the detachment correction, probably due to a stagnant flow that disrupts the streamlines over this zone. However, since only a very limited area is affected, the impact on the overall loads can be neglected.

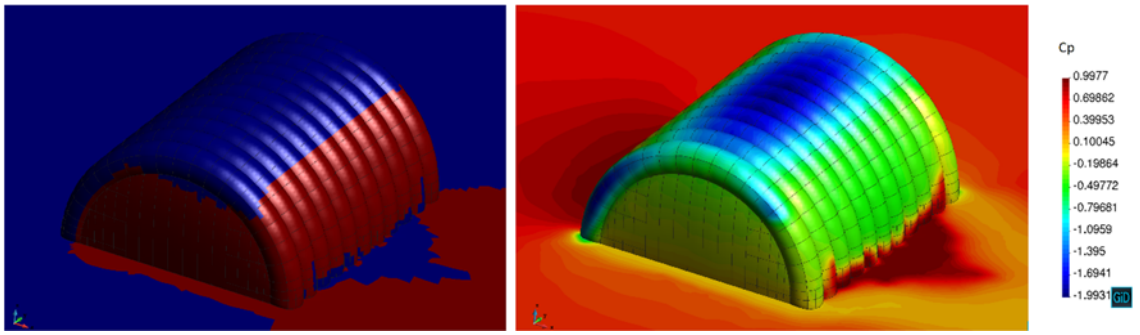

Figure 17. H20 under lateral wind. Views of the detached flow area (colored in red, left) and the corrected Cp field (right) obtained for the steady-state problem solution.

The steady pressure distribution calculated along the central tube (#6) is compared in Figure 18 with higher-fidelity CFD results and standard design loads from EN 1991-1-4. The former, provided by the manufacturer, have been calculated using the incompressible Navier-Stokes solver Tdyn [3] with Spalart-Allmaras turbulence model and law-of-the-wall boundary conditions. The geometry used takes into account the steady deformed shape of the hangar. The standard design values are calculated for a geometrically similar structure. Although building regulations do not consider neither the exact shape of the hangar nor the aeroelastic redistribution of loads that takes place, these estimations are often used for fast preliminary design when specific results are not available. Hence, it is useful to have a measure of the differences to be expected in such cases. Moving forward, for the sake of brevity, we well refer to our steady aeroelastic computation as "coupled solution" while the high-fidelity CFD solution will be named "CFD".

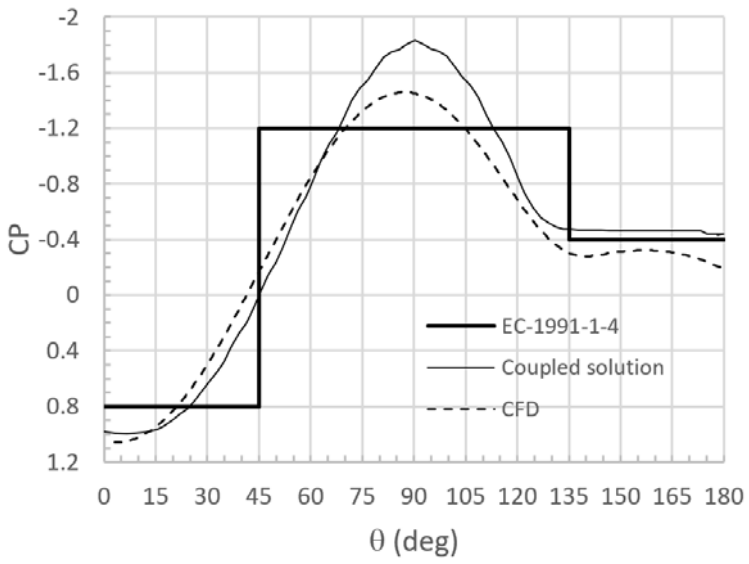

Figure 18. Cp distributions calculated along the central tube of the hangar H20 for a lateral wind condition. Comparison of coupled solution with CFD and standard design loads.

Comparing our coupled solution with CFD calculations, it is possible to observe in Figure 18 a quite good agreement for the windward face of the hangar, although the suction peak obtained is higher (about 20%) and somewhat delayed in position with respect to the CFD solution. This may be caused, to some extent, by small geometric differences between the models, but the inviscid nature of our methodology plays a major role here. Note that the trends in the comparison are similar to those already observed, for example, in Section 4.1 (see Figure 5). Regarding the detachment flow area, it is well captured by our solution and the overall comparison is satisfactory. Note that the simplified solution proposed here does not require any *a-priori* knowledge of the deformed model geometry (it is a result of the calculation). Also, the solution can be obtained in a small fraction of the time required for the CFD approach. Regarding the loads computed from the EN 1991-1-4 standard, these underestimate the maximum and minimum pressures compared to our results and the CFD solution, but the overall section load would be comparable. However, this result does not extrapolate to the entire structure. As shown below, the simplified distribution of loads in the standard (only for a few tributary areas) and the lack of aeroelastic redistribution have a large impact on the predicted structural response.

Figure 19 shows our results for the horizontal displacements (plane x-y). Positive pressures compress the windward face of the hangar while negative pressures (suction) appear on the rest of the structure. The maximum longitudinal and lateral displacements calculated are 0.25 and 0.75 meters, respectively. Regarding the vertical deformation, the roof suction causes a displacement of about 0.5 m (Figure 20, left). The reaction forces at the anchor points are also shown in Figure 20 (right), and the fabric principal stresses are displayed in Figure 21.

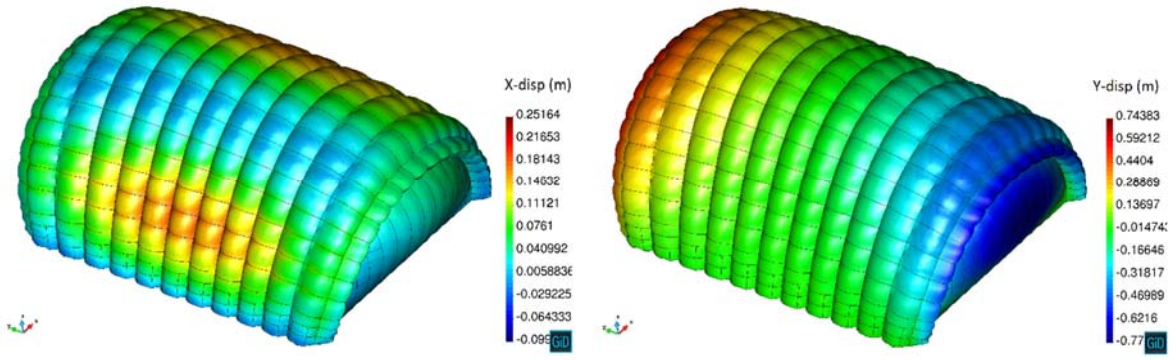

Figure 19. H20 horizontal displacements under lateral wind in the positive x-direction (displacement magnification x5).

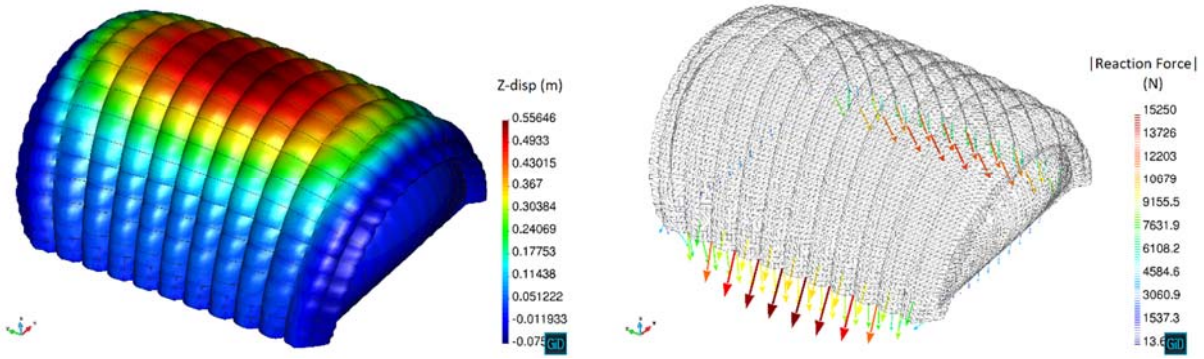

Figure 20. H20 vertical displacements and anchoring reaction forces (displacement magnification x5).

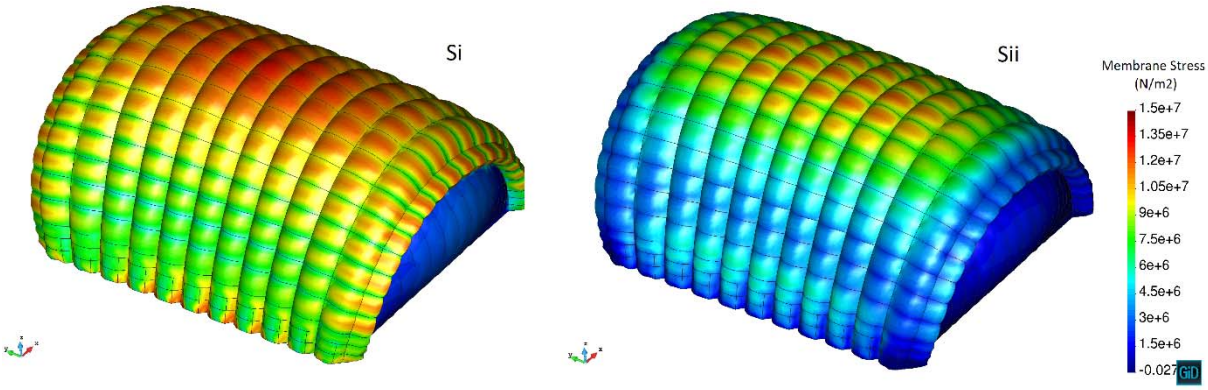

Figure 21. H20 fabric principal stresses S_1 and S_2 (displacement magnification x5).

When applying the design loads from EN 1991-1-4 to the same structural model, the maximum longitudinal and lateral displacements become 0.56 m and 2.33 m, respectively, and the roof vertical motion is 0.93 m. The maximum vertical reactions (modulus) at the anchor points along the tubes and enclosures are 23.3 kN and 12.3kN, respectively. All these values are more than twice those obtained with our coupled solution. Building regulations are, by design, conservative. This, coupled with the overly simplistic methods used to compute the design loads, results in vastly overestimated forces. According to the manufacturer's experience, the values obtained from the coupled solution and CFD (which agree reasonably well) are much more realistic for the wind conditions studied (personal communication to the authors). Since load estimations drive many critical decisions in design, it is clear that improved analysis methodologies, like the one presented here, can be very useful for developing innovative and more efficient inflatable structures.

5 CONCLUSIONS

An efficient approach for aeroelastic solution of inflatable structures has been presented. The methodology combines explicit finite-element structural dynamics and enhanced potential flow aerodynamics. The solver is a low-order panel method modified to take into account the main

characteristics of the flow around bluff shapes. To this end, the inviscid solution is used to automatically predict the detached flow areas (using the Stratford's method) and the pressure field is corrected accordingly. This procedure takes into account viscous separation effects on the wind loads acting while retaining all the advantages of the original inviscid approach.

Several validation benchmarks allowed testing the methodology on problems having similar geometric and flow characteristics in a wide range of Reynolds number. The results showed a better performance of the method for high-*Re* conditions (above critical) and when Stratford's variable S(x) is increased. The original Stratford's limits worked slightly better for lower *Re* numbers; however, in these cases the accuracy of the method depended more on whether the inviscid pressure distribution succeeded in reproducing the actual characteristics of the flow (magnitude and position of the pressure suction peak) than on the Stratford's limit employed. The tests performed show that a value S(x)=0.5 provides acceptable results over the typical range of Reynolds numbers (10^6-10^7) encountered in practice.

In addition, the numerical results show that for some problems and Reynolds numbers, the lack of pressure correction upstream the separation point can degrade the accuracy of the results. By construction, the method does not take into account the reduction of the suction peak that occurs as the separation point moves upstream with changing conditions (in that area the purely potential solution is retained). This error is often larger than the uncertainty introduced by the choice of S(x), and should be the primary focus for future improvements. In this regard, an enhanced version of the model that applies empirical pressure correction upstream of the separation area (based on the extent of the detached region) is currently under development. If successful, this should yield important improvements to the accuracy of the method.

Overall, the results obtained indicate that the enhanced aerodynamic model can estimate wind loads on inflatable bluff structures with reasonable accuracy, at a small fraction of cost of high-fidelity CFD approaches. In addition, the method can be used to improve the design process of real inflatable structures by providing inexpensive aeroelastic solutions. All in all, the solution approach developed strikes a balance between accuracy and computational cost that makes it suitable for routine design tasks. It can prove especially useful in the design of structures with unconventional characteristics, where standard design practices become unreliable.

ACKNOWLEDGEMENTS

Special thanks are given to BuildAir Inflatable Structures Solutions S. A. (www.buildair.com) for providing analysis models, test data and many other useful inputs during the development of this work.

REFERENCES

1. Veldman, S.L., Vermeeren, C. A. J. R. . *Inflatable structures in aerospace engineering-an overview*. in *Spacecraft Structures, Materials and Mechanical Testing*. 2001.
2. Martens, B., Tschuppik, W. M. *Exploring the Design and Fabrication of Inflatables*. in *ACADIA 2006: Synthetic Landscapes*. 2006.
3. Oñate, E., Flores, F. G., Marcipar, J., *Membrane Structures Formed by Low Pressure Inflatable Tubes. New Analysis Methods and Recent Constructions*, in *Textile Composites and Inflatable Structures II*. 2008, Springer: Dordrecht. p. 163-196.
4. Stimpfle, B. *Structural Air-Pneumatic Structures*. in *Textile Composites and Inflatable Structures II*. 2008. Springer, Dordrecht.
5. Skouras, M., Thomaszewski, B., Kaufmann, P., Garg, A., Bickel, B., Grinspun, E., Gross, M., *Designing inflatable structures.* ACM Transactions on Graphics (TOG), 2014. **33**(4): p. 10.
6. Aboshio, A., Ye, J., *Numerical study of the dynamic response of Inflatable Offshore Fender Barrier Structures using the Coupled Eulerian-Lagrangian discretization technique.* Ocean Engineering, 2016. **112**: p. 265-276.
7. Lipecki, T., Jamińska, P., *Issues of contemporary wind engineering and aerodynamics of building structures.* Budownictwo i Architektura, 2016. **15**(3).
8. Chatzikonstantinou, T., *Numerical analysis of three-dimensional non rigid wings.* AIAA paper 89-0907, Aerodynamic Decelerator Systems Technology Conference, 10 th, Cocoa Beach, FL, 1989.
9. Ross, J.C., *Computational Aerodynamics in the Design and Analysis of Ram-Air-Inflated Wings.* AIAA Paper 1991-1548, 1993: p. 10-13.
10. Chatzikonstantinou, T., *Recent advances in the numerical analysis of ram air wings - The three dimensional simulation code 'PARA3D'".* 12th Aerodynamic Decelerator Systems Technology Conference, 1993.
11. Chatzikonstantinou, T., *Problems in ram air wing modeling and their solution in the three dimensional simulation code 'PARA3D'.* 15th Aerodynamic Decelerator Systems Technology Conference, Aerodynamic Decelerator Systems Technology Conferences, paper AIAA-99-1716, 1999.
12. van Opstal, T.M., van Brummelen, E. H., de Borst, R., Lewis, M. R., *A finite-element/boundary-element method for large-displacement fluid-structure interaction.* Computational Mechanics,, 2012. **50**(6): p. 779-788.
13. van Opstal, T., van Brummelen, E. *Model comparison for inflatables using boundary element techniques*. in *First ECCOMAS young investigators conference*. 2012.
14. van Opstal, T.M., van Brummelen, E. H., van Zwieten, G. J. , *A finite-element/boundary-element method for three-dimensional, large-displacement fluid-structure-interaction.* Computer Methods in Applied Mechanics and Engineering, 2015. **284**: p. 637-663.
15. Gharakhani, A., *A Survey of Grid-Free Methods for the Simulation of 3-D Incompressible Flows in Bounded Domains.* Sandia National Laboratory Report, SAND97-2256, 1997.
16. Voutsinas, S.G., *Vortex methods in aeronautics: how to make things work.* International Journal of Computational Fluid Dynamics, 2006. **20**(1): p. 3-18.

17. Winckelmans, G.S., *Vortex methods*, in *Encyclopedia of Computational Mechanics*. 2018. p. 1-24.
18. Strickland, J.H., Higuchi, H., Homicz, G. F., Porter, V. L., Gossler, A. A., *VIPAR version 1.0*. SANDIA report SAND2002-2174, 2002.
19. Ould-Salihi, M.L., Cottet, G. H., El Hamraoui, M., *Blending finite-difference and vortex methods for incompressible flow computations.* SIAM Journal on Scientific Computing, 2001. **22**(5): p. 1655-1674.
20. Stock, M.J., *Summary of Vortex method Literature.* 2006.
21. Tezduyar, T.E., *Interface-tracking and interface-capturing techniques for finite element computation of moving boundaries and interfaces.* Computer Methods in Applied Mechanics and Engineering, 2006. **195**(23-24): p. 2983-3000.
22. Van Loon, R., Anderson, P. D., Van de Vosse, F. N., Sherwin, S. J., *Comparison of various fluid-structure interaction methods for deformable bodies.* Computers and Structures, 2007. **85**(11-14): p. 833-843.
23. Farhat, C., Lakshminarayan, V. K., *An ALE formulation of embedded boundary methods for tracking boundary layers in turbulent fluid-structure interaction problems.* Journal of Computational Physics, 2014. **263**: p. 53-70.
24. Tezduyar, T.E., Behr, M., Mittal, S., Liou, J., *A new strategy for finite element computations involving moving boundaries and interfaces-the deforming-spatial-domain/space-time procedure: II. Computation of free-surface flows, two-liquid flows, and flows with drifting cylinders.* Computer Methods in Applied Mechanics and Engineering, 1992. **94**(3): p. 353-371.
25. Tezduyar, T.E., Behr, M., Liou, J., *A new strategy for fnite element computations involving moving boundaries and interfaces: the deforming-spatial-domain/space time procedure: I. The concept and the preliminary numerical tests.* Computer Methods in Applied Mechanics and Engineering, 1992. **94**(3): p. 339-351.
26. Wüchner, R., Wang, T., Sicklinger, S., Schmidt, R., Apostolatos, A., Bletzinger, K. U., *Partitioned multifield simulation for analysis and design of free-form, light-weight structures subject to wind*, in *In Advances in Computational Mechanics*. 2013: San Diego.
27. Wüchner, R., Kupzok, A., Bletzinger, K. U., *A framework for stabilized partitioned analysis of thin membrane-wind interaction.* International Journal for Numerical Methods in Fluids, 2007. **54**(6-8): p. 945-963.
28. Li, B., Habbal, F., Ortiz, M., *Optimal transportation meshfree approximation schemes for fluid and plastic flows.* International Journal for Numerical Methods in Engineering, 2010. **83**(12): p. 1541-1579.
29. York, A.R., Sulsky, D., & Schreyer, H. L., *Fluid-membrane interaction based on the material point method.* International Journal for Numerical Methods in Engineering, 2000. **48**(6): p. 901-924.
30. Hirth, A., Haufe, A., Olovsson, L. , *Airbag simulation with LS-DYNA past-present-future.* Presentation in LS-DYNA Anwenderforum, Frankenthal, 2007.
31. Wüchner, R., Kupzok, A., Bletzinger, K. U., *Analysis of Free Form Membranes Subject to Wind Using FSI*, in *Textile Composites and Inflatable Structures II*. 2008, Springer: Dordrecht. p. 141-161.
32. El Hami, A., Radi, B, *Fluid-Structure Interaction with Ansys/Fluent*, in *Fluid-Structure Interactions and Uncertainties*, A. El Hami, Radi, B., Editor. 2017.
33. Flores, R., Ortega, E., Onate, E., *Simple and efficient numerical tools for the analysis of parachutes.* Engineering Computations, 2014. **31**(5).
34. Ortega, E., Flores, R., Pons-Prats, J., *Ram-Air Parachute Simulation with Panel Methods and Staggered Coupling.* Journal of Aircraft, 2017. **54**(2): p. 807-814.

35. De la Torre, D., Ortega, E., Flores, R., *PARACHUTES. A computer program for calculating ram-air parachutes. User's manual.* CIMNE publication, 2015.
36. Cook, N., *Designers' Guide to EN 1991-1-4 Eurocode 1: Actions on structures, general actions part 1-4. Wind actions.* Thomas Telford Publishing, 2007.
37. Cebeci, T., Mosinskis, G. J., Smith, A. M. O., *Calculation of Viscous Drag and Turbulent Boundary-Layer Separation on Two-Dimensional and Axisymetric Bodies in Incompressible Flows.* Report MDC-J0973-01, Douglas Aircraft Co, 1970.
38. Gerhart, P.M., Bober, L. J., *Comparison of several methods for predicting separation in a compressible turbulent boundary layer.* NASA TM X-3102, 1974.
39. Stratford, B.S., *The prediction of separation of the turbulent boundary layer.* Journal of Fluid Mechanics, 1959. **5**(1): p. 1-16.
40. Smith, A.M.O., *Stratford's turbulent separation criterion for axially-symmetric flows.* Journal of Applied Mathematics and Physics (ZAMP), 1977. **28**(5): p. 929-939.
41. Michel, R., *Etude de la Transition sur les Profiles d'Aile; Etablissement d'un Critére de Determination de Point de Transition et Calcul de la Trainee de Profile Incompressible.* ONERA Report, 1951. **1**.
42. Kuethe, A.M., Chow, C. Y., *Foundations of Aerodynamics. Bases of Aerodynamics Design.* 5 ed.: John Wiley & Sons, Inc.
43. Cebeci, T., Mosinskis, G. J., Smith, A. M. O, *Calculation of separation points in incompressible turbulent flows.* Journal of Aircraft, 1972. **9**(9): p. 618-624.
44. Hoffmann, K.A. and S.T. Chiang, *Computational fluid dynamics. Volume I.* 2000: Engineering Education System. Wichita, USA.
45. Cebeci, T., Carr, L. W., *A computer program for calculating laminar and turbulent boundary layers for two-dimensional time-dependent flows.* NASA TM 78470, 1978.
46. Jones, G.W., Walker, R. W., *Aerodynamic forces on a stationary and oscillating circular cylinder at high Reynolds numbers.* NASA Technical Report R-300, 1969.
47. Schubauer, G.B., *Air flow in the boundary layer of an elliptic cylinder.* NACA Technical Report 652, 1939.
48. Hoerner, S.F., *Fluid-dynamic drag: practical information on aerodynamic drag and hydrodynamic resistance*. 1965: Midland Park, NJ: Hoerner Fluid Dynamics.
49. *ULITES. Ultra-lightweight structures with integrated photovoltaic solar cells: design, analysis and application to an emergency shelter prototype.* . Ref. 314891. Seventh Framework Program, European Comission, 01/12/2012-31/05/2015.
50. Bartolli, G.A., D., Giachetti, A., Pigolotti, L., *Report on boundary layer wind tunnel tests on rigid and flexible models for uLites project.* CRIACIV, University of Florence, 2014.
51. Roshko, A., *Experiments on the flow past a circular cylinder at very high Reynolds number.* Journal of Fluid Mechanics, 1961. **10**(3): p. 345-356.
52. *Buidair's outstanding projects: hangars H20 Poland*. 07/28/2018]; Available from: http://www.buildair.com/projects-delivered/hangers-h20-poland/.
53. Cuartero Zaragozá, E., *Estudio y aplicación de un método acoplado fluido-estructura al análisis de estructuras de membrana hinchables*, in *Departament d'Enginyeria Civil i Ambiental. Escola Tècnica Superior d'Enginyers de Camins, Canals i Ports de Barcelona (ETSECCPB)*. 2017, Master Thesis. Universitat Politècnica de Catalunya.